

Do Molecular Geometries Change Under Vibrational Strong Coupling?

Thomas Schnappinger* and Markus Kowalewski†

Department of Physics, Stockholm University, AlbaNova University Center, SE-106 91 Stockholm, Sweden

(Dated: May 28, 2024)

As pioneering experiments have shown, strong vibrational coupling between molecular vibrations and light modes in an optical cavity can significantly alter molecular properties and even affect chemical reactivity. However, the current theoretical description is limited and far from complete. To explore the origin of this exciting observation, we investigate how the molecular structure changes under strong light-matter coupling using an *ab-initio* method based on the cavity Born-Oppenheimer Hartree-Fock ansatz. By optimizing H₂O and H₂O₂ resonantly coupled to cavity modes, we study the importance of reorientation and geometric relaxation. In addition, we show that the inclusion of one or two cavity modes can change the observed results. On the basis of our findings, we derive a simple concept to estimate the effect of the cavity interaction on the molecular geometry using the molecular polarizability and the dipole moments.

I. INTRODUCTION

When molecules are placed in a non-classical photonic environment present in optical or nanoplasmonic cavities, it is possible to form strong light-matter-coupled hybrid states called polaritons [1–6]. The control of the photonic environment allows to couple the cavity photon modes to vibrational or electronic transitions in molecules, called vibrational-strong coupling (VSC) or electronic-strong coupling (ESC), respectively. Both types of strong coupling can be an effective tool for modifying molecular properties and offer a possible novel approach to control chemical reactions using optical resonators. The experimental advances reported cover a wide range of applications, from manipulating the selectivity of organic reactions [7–9], changing the ionic conductivity of water [10] to even influencing enzymatic activity [11, 12]. Driven by these experimental advances, considerable efforts have been made to develop theories that elucidate the mechanisms governing polaritonic chemistry. Even so, the current theoretical description is limited and far from complete. However, in recent years, a substantial number of studies using different theoretical approaches have proposed that a variety of additional reactions can be enhanced, inhibited, or controlled [13–25]. In particular, the combination of electronic structure methods and quantum electrodynamics [26–34] has significantly improved theoretical understanding and will hopefully help close the existing gaps between theory and experiment. Most of these studies model cavity-induced electronic structure changes using a single molecule coupled to a single-cavity mode in the strong-coupling limit. In almost every example, both a fixed orientation relative to the polarization axes of the cavity mode and fixed molecular geometries are assumed, despite the fact that the coupling strengths used are quite large.

In this work, we use the cavity Born-Oppenheimer

Hartree-Fock (CBO-HF) ansatz [31] together with analytical gradients [35] to optimize H₂O and H₂O₂ resonantly coupled to one and two cavity photon modes. The CBO-HF ansatz is capable of describing the electronic ground state of single molecules, as well as an ensemble of molecules coupled to an optical cavity under VSCs conditions [31, 33, 36]. By performing the optimizing the geometries in the laboratory frame together with the polarization vectors of the cavity, we are able to study both the orientation and the relaxation of the internal coordinates of the molecules induced by the interaction with the cavity photon modes. Furthermore, we calculate vibro-polaritonic IR spectra [35] within the harmonic approximation, we allow for the verification of the structures found as real minima and to analyze in detail the formed polaritonic states. As will become clear in the remainder of this article, without a physical mechanism to fix the orientation, molecules inside an optical cavity will orient and change their geometry depending on the coupling strength. Furthermore, these observed effects will vary if one- or two-cavity orthogonal photon modes are included in the simulation. The main results of this work are indication that some theoretical studies in the literature may overestimate the cavity-induced effects on the ground-state chemistry. Finally, we establish a useful and straightforward connection between the molecular polarizability and dipole moment and the expected reorientation and relaxation of a molecule coupled to an optical cavity.

II. RESULTS & DISCUSSION

A. Optimization of H₂O embedded in a cavity

As a first example, we optimize a H₂O molecule coupled to one photon mode of an optical cavity. The cavity frequency ω_m is resonant with the bending mode, which has a field-free vibrational frequency of 1744 cm⁻¹, and the cavity polarization axis \mathbf{e} is aligned with the x axis of the laboratory frame. Fig. 1 shows the optimized parameters for the coupled molecular cavity system as a

* thomas.schnappinger@fysik.su.se

† markus.kowalewski@fysik.su.se

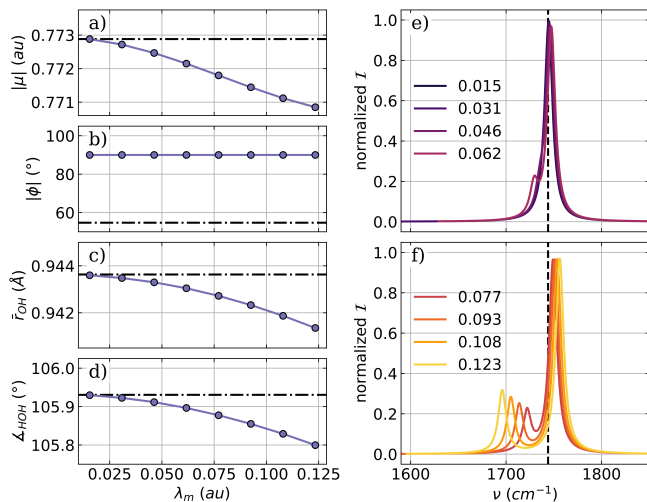


FIG. 1. Optimized parameters of a H₂O molecule coupled to a single photon mode of an optical cavity as a function of the coupling strength λ_m . a) Magnitude of the dipole moment $|\mu|$ b) the angle ϕ between the polarization axis of the cavity and the dipole moment, c) averaged OH bond length and d) bond angle. The dashed-dotted lines in a)-d) indicate the initial values. Relevant parts of the vibro-polaritonic IR spectra for different coupling strengths (color-coded) are shown in e) and f). The cavity frequency ω_m is 1744 cm^{-1} shown as a black dashed line in e) and f). The cavity coupling λ_m increases from 0.015 au to 0.123 au and the cavity polarization axis is $e = (1, 0, 0)$.

function of the coupling strength λ_m and the corresponding vibro-polaritonic IR spectra in the region of the H₂O bending mode.

For the optimized single-mode cavity-H₂O system, the magnitude of the dipole $|\langle\mu\rangle|$ moment, shown in Fig. 1 a), is only slightly reduced with increasing λ_m . This rather small change is consistent with the observed small decrease in both the OH bond length (Fig. 1 c)) and bond angle (Fig. 1 d)) even at high coupling strengths. The only system parameter significantly affected by VSC is the relative orientation of the molecular dipole moment and the polarization axis of the cavity mode visualized as the angle ϕ between them in Fig. 1 b). For the arbitrary chosen initial configuration, ϕ has a value of about 55° (dashed dotted line), which changes to exactly 90° after optimization, regardless of the coupling strength. The interaction with the photon field leads to an orientation of the molecule so that not only the dipole moment but also the molecular plan is orthogonal to the polarization axis. The relevant parts of the vibro-polaritonic IR spectra for the optimized water-cavity system are shown in Fig. 1 e) and f) for different coupling strengths. Given the orientation of the dipole moment perpendicular to the cavity polarization axis, one would expect no hybrid photonic states to be formed because of the lack of dipole-cavity interaction. This assumption holds for lower coupling strengths below 0.062 au, shown in Fig. 1 e). Within the used broadening of 10 cm^{-1} , only a single peak is

observed, almost unshifted to the field-free value (black dashed line). For $\lambda_m = 0.062$ au a small shoulder appears at a slightly lower frequency, the bright purple line in Fig. 1 e). If the coupling is further increased, as shown in Fig. 1 f), this shoulder becomes a separate peak with increasing intensities and shifts to lower frequencies with increasing λ_m . As introduced in our early work [35], the normal mode component that describes the change in the classical photon displacement field is a measure of how much photon character the corresponding transition is. The main peak in all shown vibro-polaritonic IR spectra has no photonic character and can be described as a pure molecular transition corresponding to the bending mode. The smaller peak at higher coupling strengths is predominantly photonic, and we do not see the formation of a typical hybrid matter-photon lower polariton (LP) state and upper polariton (UP) state here. This can be explained by a rotational motion of the H₂O molecule. Due to the confinement of the cavity, this motion is not a free rotation anymore. This motion creates a dipole moment parallel to the cavity polarization axis, which leads to a coupling with the photon mode. Due to this coupling, the photonic transition gains intensity and shifts to lower frequencies. More details and a thorough analysis of the photonic characters of all relevant transitions can be found in the Supporting Information.

Next, we discuss the optimization results for H₂O coupled to two cavity modes of orthogonal polarization with the same frequency, effectively modeling a Fabry-Pérot-like setup. In practice, we use the same cavity frequency and coupling strength for both modes and take the same values as for the single-mode case. The polarization axes are aligned with the x axis (e_1) and the y axis (e_2) of the laboratory frame. The optimized parameters as a function of the coupling strength λ_m and the corresponding vibro-polaritonic IR spectra in the region of the H₂O bending mode are shown in Fig. 2

When the optimized parameters are compared for the single-mode case and the two-mode case, some similarities but also distinct differences are observed. The change in magnitude of the dipole moment, shown in Fig. 2 a), is nearly one order of magnitude smaller for the two-mode optimization. In contrast, the OH bond length (Fig. 2 c)) and the bond angle (Fig. 2 d)) are more strongly influenced by the coupling to two cavity modes. In particular, the change in the bond angle is significantly larger compared to the case of a single mode, although it increases only by 1.5° for the highest coupling strength. Again, the most significant changes due to optimization are the relative orientations of the molecular dipole moment with respect to the cavity-mode polarization axes. The corresponding angles ϕ for e_1 and e_2 are shown in Fig. 2 b). Starting from a configuration where both e_1 and e_2 are in the molecular plane but not aligned with the dipole moment, the optimization reorients the molecule independently of the coupling strength so that e_1 is parallel to the dipole moment, while e_2 is orthogonal to the dipole moment and the molecular plane. The correspond-

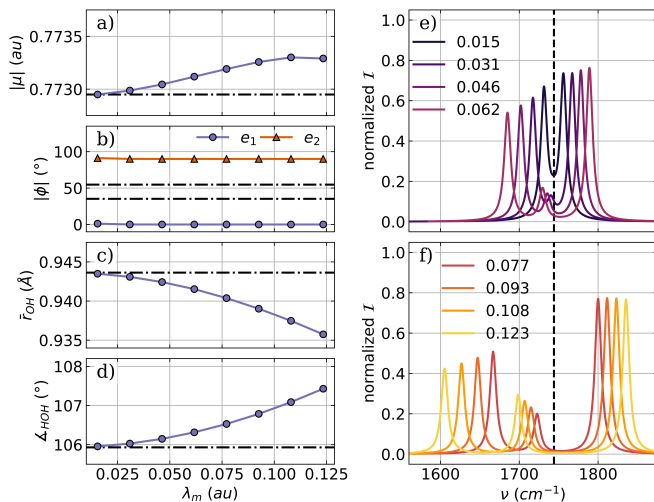


FIG. 2. Optimized parameters of a H_2O molecule coupled to two orthogonal cavity photon modes as a function of the coupling strength λ_m . a) Magnitude of the dipole moment $|\mu|$ b) the two angle ϕ between the polarization axes of the cavity and the dipole moment of the molecule, c) averaged OH bond length and d) the bond angle. The dashed-dotted lines indicate the initial values in a)-d). The relevant part of the vibro-polaritonic IR spectra for different coupling strengths (color-coded) is shown in e) and f). The cavity frequency ω_m is 1744 cm^{-1} shown as a black dashed line in e) and f). The cavity coupling λ_m increases from 0.015 au to 0.123 au and the cavity polarization axes are $\mathbf{e}_1 = (1, 0, 0)$ and $\mathbf{e}_2 = (0, 1, 0)$.

ing vibro-polaritonic IR spectra for the optimized water-cavity system are shown in Fig. 2 e) and f) for different coupling strengths. Already, for the lowest coupling strength $\lambda_m = 0.015\text{ au}$ in Fig. 2 e), a splitting into a LP transition and a UP transition is observed. The corresponding normal modes clearly show a hybridization of the vibrational transition and the cavity photon mode with the polarization axis \mathbf{e}_1 . As λ_m increases, the Rabi splitting between the LP and UP transitions increases and becomes more asymmetric, consistent with our previous work [35, 36]. At the same time, a third weaker peak between the LP and UP transitions becomes visible. Similarly to the single-mode case, this peak is due to the coupling between a specific constricted rotational degree of freedom and the photon mode with the polarization axis \mathbf{e}_2 . Due to this coupling, the photonic transition gains intensity and shifts to low frequencies with increasing coupling strength. More information on the photonic characters of all relevant transitions can be found in the Supporting Information.

To gain more insight into the underlying driving force for the energetically favorable orientation, we discuss how VSC modifies the polarizability α and the dipole self-energy (DSE) contribution. The principal components of the polarizability tensor α and the change in the DSE contribution are shown in Fig. 3 as a function of the coupling strength for both optimized H_2O -cavity systems.

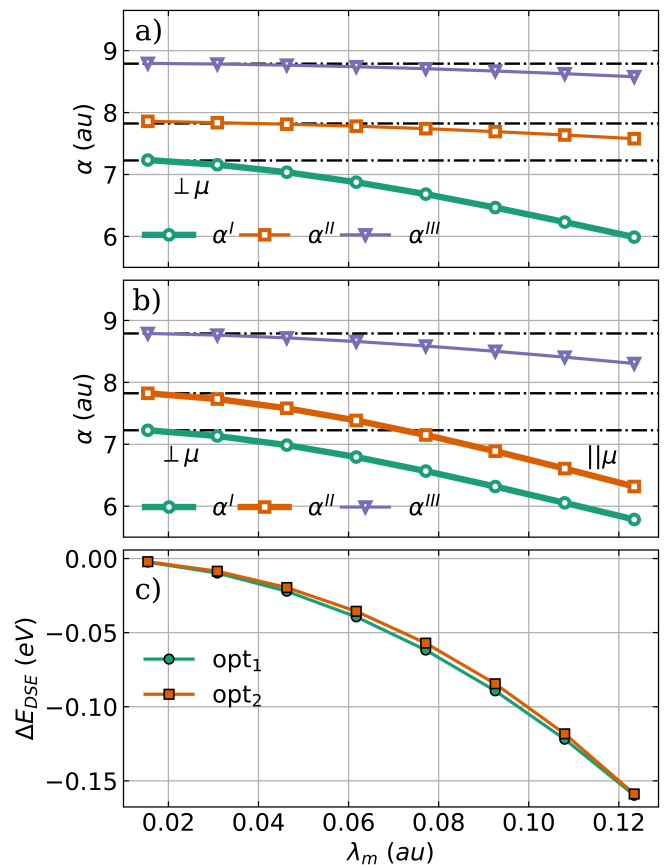


FIG. 3. Principal components of the polarizability tensor α as a function of the coupling strength λ_m for optimized H_2O structures coupled to a) a single cavity mode and to b) two orthogonal cavity modes. The bold line indicates the component aligned with the cavity polarization axes, and the black dashed dotted lines represent the field-free principal components of the polarizability. c) Change in DSE contribution as a function of the coupling strength λ_m compared to the initial H_2O geometry for the single-mode case (green) and the two-mode case (orange). The cavity frequency ω_m is 1744 cm^{-1} .

In the single-mode case shown in Fig. 3 a) and the two-mode case shown in Fig. 3 b) all three principal components of α are reduced with increasing coupling strength or, in other words, the interaction with the photon mode contracts the electronic density. Therefore, it is logical that the components aligned with the cavity polarization axes (highlighted in bold) are the most affected. These components already have the smallest value in the field-free case, and the optimization reorients the molecule so that these components align with the cavity polarization axes. For H_2O these are the components orthogonal to the molecular plane corresponding to the green lines in Fig. 3 a) and b) and the one parallel to the molecular dipole moment corresponding to the orange lines in Fig. 3 a) and b). As shown in Fig. 3 c), the observed reorientation also minimizes the DSE contribution to the coupled cavity-molecule system. This is in agreement

with our previous work [31] and a recent study by Liebenthal and DePrince [37]. In general, reorientation can be rationalized as an effective way to reduce molecular polarizability along the cavity polarization axes and thus minimizing the DSE contribution.

All results presented for the optimization of H_2O resonantly coupled to a single or two orthogonal cavity photon modes show that, without restriction of the rotational degrees of freedom, the cavity interaction leads to a reorientation of the molecule. This rotational motion occurs for all coupling strengths and is more pronounced than changes in the internal coordinates of H_2O . For higher coupling strengths, the rotational effects even become visible in the vibro-polaritonic IR spectra.

B. Optimization of H_2O_2 embedded in a cavity

The optimization of a H_2O_2 molecule coupled to a single photon mode and two to orthogonal photon modes serves as the second example. The cavity is resonant with the asymmetric bending mode of 1491 cm^{-1} , and the cavity polarization axis \mathbf{e} in the case of a single mode is aligned with the molecular dipole moment, which corresponds to the z axis of the laboratory frame. The optimized parameters for the coupled molecular cavity system as a function of the coupling strength λ_m and the relevant part of the corresponding vibro-polaritonic IR spectra are shown in Fig. 4.

Regardless of the coupling strength used, the dipole moment of H_2O_2 remains aligned with the polarization axis of the single cavity mode, as shown in Fig. 4 b). However, its size decreases significantly with increasing coupling up to the situation where the dipole moment is zero at $\lambda_m = 0.150\text{ au}$ (see Fig. 4 a)). This large change in the dipole moment with the increasing coupling strength is induced by an increase in the dihedral angle, leading to a planarization of H_2O_2 (see orange line Fig. 4 d)). For $\lambda_m = 0.150\text{ au}$ the H_2O_2 molecule becomes completely planar in a *trans* configuration, which results in a zero dipole moment. Note that for this *trans* structure, the cavity polarization axis is orthogonal with respect to the molecular plane, very similar to the H_2O case. In contrast, the bond lengths and the averaged bond angle shown in Fig. 4 c) and Fig. 4 d), respectively, remain nearly constant for increasing couplings strengths. The observed change in the molecular geometry due to the cavity interaction can be clearly seen in the corresponding vibro-polaritonic IR spectra, shown in Fig. 4 e) and f) for different coupling strengths. Details about the photonic characters of all relevant transitions can be found in the Supporting Information. For smaller values of λ_m , as depicted in Fig. 4 e), there is a clear splitting into a LP transition and a UP transition, which increases with increasing coupling strength. If λ_m is further increased, the changes in dipole moment and dihedral angle are more pronounced, which changes the vibro-polaritonic IR spectra, see Fig. 4 f). These spectra are characterized

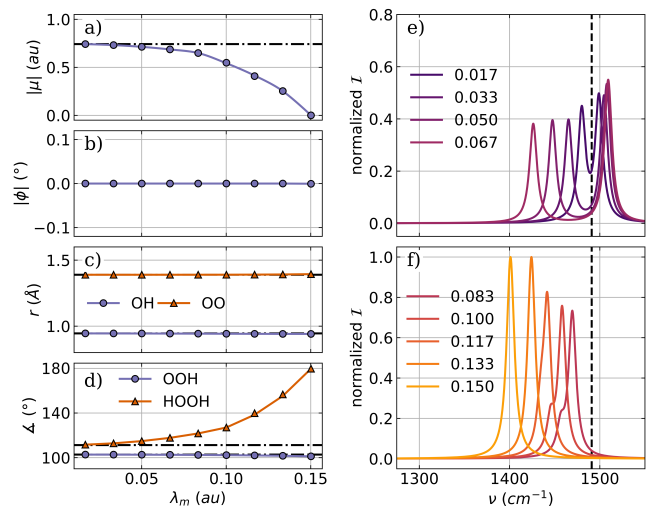


FIG. 4. Optimized parameters of a H_2O_2 molecule coupled to a single photon mode of an optical cavity as a function of the coupling strength λ_m . a) Magnitude of the dipole moment $|\mu|$ b) the angle ϕ between the polarization axis of the cavity and the dipole moment of the molecule, c) averaged OH bond length (purple) and OO bond length (orange) and d) the averaged bond angle (purple) as well as the dihedral angle (orange). The dashed-dotted lines in a)-d) indicate the initial values. Relevant parts of the vibro-polaritonic IR spectra for different coupling strengths (color-coded) are shown in e) and f). The cavity frequency ω_m is 1491 cm^{-1} shown as a black dashed line in e) and f). The cavity coupling λ_m increases from 0.017 au to 0.150 au and the cavity polarization axis is $\mathbf{e} = (0, 0, 1)$.

by a single peak that is a pure molecular transition but is red-shifted relative to the field-free asymmetric bending mode. For a coupling strength below 0.13 au a small shoulder a slightly lower frequency is present. This signal has a photonic character and is visible due to the weak coupling of the photon mode with the twisting mode in H_2O_2 at 424 cm^{-1} . This mode is the most intense transition in the field-free spectrum and is characterized by a change in the dihedral angle of H_2O_2 . Similarly to the rotational motion observed in H_2O , this twisting mode induces a dipole moment parallel to the polarization axis of the cavity. However, as the coupling increases further and H_2O_2 becomes more planar, this coupling weakens, and only the single molecular peak remains visible.

To optimize the H_2O_2 molecule coupled to a two mode cavity, we add a second orthogonal cavity mode with the same frequency and coupling strength. The two polarization axes are aligned with the z axis (\mathbf{e}_1) and the x axis (\mathbf{e}_2) of the laboratory frame. The optimized parameters as a function of the coupling strength λ_m and the relevant part of the vibro-polaritonic IR spectra are shown in Fig. 5

Optimization of H_2O_2 coupled to a two-mode cavity setup leads to similar but significantly weaker changes than in the case of coupling to a single cavity mode. The dipole moment is reduced with increasing coupling

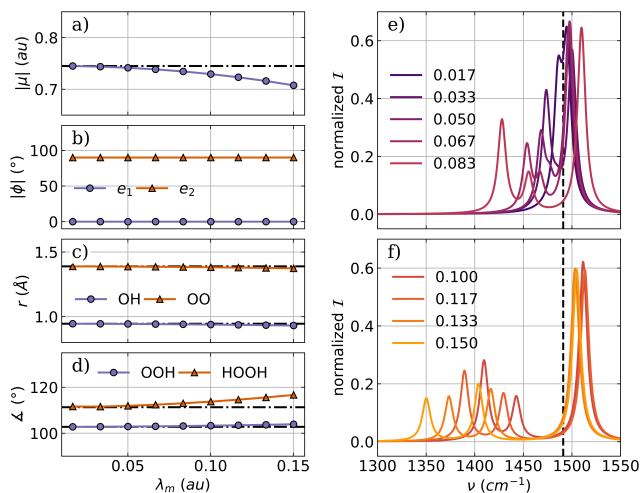


FIG. 5. Optimized parameters of a H_2O_2 molecule coupled to two orthogonal cavity photon modes as a function of the coupling strength λ_m . a) Magnitude of the dipole moment $|\mu|$ b) the angle ϕ between the cavity polarization axes and the dipole moment of the molecule, c) averaged OH bond length (purple) and OO bond length (orange) and d) the averaged bond angle (purple) as well as the dihedral angle (orange). The dashed-dotted lines in a)-d) indicate the initial values. Relevant parts of the vibro-polaritonic IR spectra for different coupling strengths (color-coded) are shown in e) and f). The cavity frequency ω_m is 1491 cm^{-1} shown as a black dashed line in e) and f). The cavity coupling λ_m increases from 0.017 au to 0.150 au and the cavity polarization axes are $\mathbf{e}_1 = (0, 0, 1)$ and $\mathbf{e}_2 = (1, 0, 0)$.

strength, see Fig. 5 a), while the dihedral angle is simultaneously increased, see Fig. 5 d) orange line. The other internal coordinates of H_2O_2 , shown in Fig. 2 c) and d), are slightly more affected in the two-mode case, but still in a rather insignificant way. Similarly to the single-mode coupling, we do not observe any reorientation of the H_2O_2 dipole moment with respect to the polarization axes for the two-mode case due to the chosen orientation of the initial geometry. The dipole moment is parallel to the polarization axis \mathbf{e}_1 and therefore orthogonal to the other, as visualized in Fig. 5 b). Next, we discuss the vibro-polaritonic IR spectra of the optimized H_2O_2 molecule coupled to a two-mode cavity. Fig. 5 e) shows spectra for smaller coupling strengths, which can be roughly divided into two groups. When λ_m is less than 0.05 au , a weak Rabi splitting is observed. The LP transition and the UP transition are formed by the asymmetric bending mode and the cavity photon mode with the polarization axis \mathbf{e}_1 . This "standard" pair of LP and UP is present in all spectra and the Rabi splitting increases with increasing coupling strength, see Fig. 5 e) and f). But similar to the case of H_2O coupled with two cavity modes, a third weaker signal is present first as a shoulder ($\lambda_m = 0.05 \text{ au}$ Fig. 5 e)) later as a distinct peak as shown in Fig. 5 f). This weaker "middle" signal is mostly photonic and is characterized by the cavity pho-

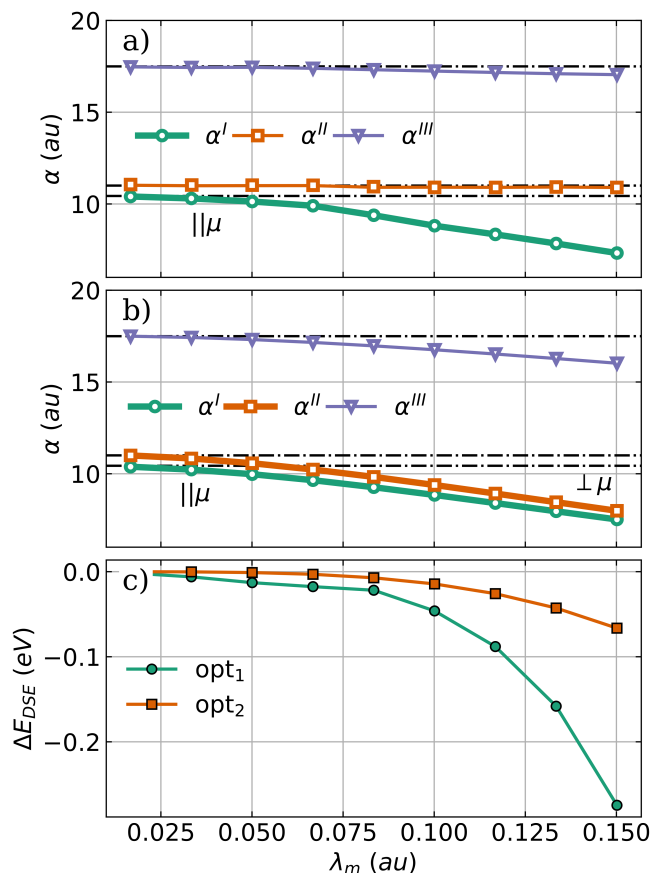


FIG. 6. Principal components of the polarizability α as a function of the coupling strength λ_m for optimized H_2O_2 structures coupled to a single cavity mode a) and to two cavity modes b). The bold line indicates the component aligned with the cavity polarization axes, and the black dashed dotted lines represent the field-free principal components of the polarizability. c) Change in DSE contribution as a function of the coupling strength λ_m compared to the initial H_2O_2 geometry for the single-mode case (green) and the two-mode case (orange). The cavity frequency ω_m is resonant with the bending mode (1491 cm^{-1}).

ton mode with the polarization axis \mathbf{e}_2 . In line with the single-mode case, this transition is due to a weak coupling to the twisting mode in H_2O_2 for higher coupling strengths. A visualization of the photonic characters of all relevant transitions can be found in the Supporting Information.

As discussed for the optimization of H_2O , we also want to understand the observed changes in H_2O_2 due to the cavity interaction by analyzing the polarizability α and the DSE contribution. The principal components of the polarizability tensor α and the change in the DSE contribution are shown in Fig. 6 as a function of the coupling strength for both optimized H_2O_2 -cavity systems.

Consistent with the H_2O results shown in Fig. 3, in both the single-mode case and the two-mode case, all three principal components of the polarizability α de-

crease with increasing coupling strength, see Fig. 6 a) and b). The components aligned with the cavity polarization axes, highlighted in bold, are more strongly reduced by the cavity interaction, while especially for the single-mode case Fig. 6 a) the other two components remain almost unchanged. We do not see reorientation of H_2O_2 for the cavity polarization axes studied in the single-mode and two-mode cases, since for the chosen molecular orientation the axes are already aligned with the smallest polarizability components α^I and α^{II} . Consequently, the observed reduction in polarizability is achieved only by geometrical changes and the direct response of the electronic structure to the cavity photon field. These geometrical changes and the electronic response also minimizes the DSE contribution. The change in E_{DSE} is plotted as a function of λ_m in Fig. 6 c). Interestingly, the energy change is much larger for the single-mode case (green line) compared to the two-mode case (orange line), although the change in α is comparable. To explain this, we have to consider that the total DSE contribution can be separated into a one-electron and two-electron part [31, 33, 36]. The behavior of the one-electron contribution, and usually larger part, can be estimated by the polarizability, while the two-electron contribution is defined by the dipole moment. Since in the single-mode case H_2O_2 planarizes with increasing coupling strength, its dipole moment vanishes and the two-electron part of the DSE is zero. Consequently, in the single-mode case, the change in DSE reflects both the decrease in polarizability and the decrease in the dipole moment. The present result for the optimization of H_2O and H_2O_2 coupled to an optical cavity clearly shows that not only the dipole moment of the molecule is important, but also the polarizability is a decisive factor in determining the influence of the molecule-cavity interaction.

III. CONCLUSION

To conclude, we studied the importance of geometry relaxation and relative orientation in the context of molecules coupled to the photon modes of optical cavities. Both effects are currently neglected in most computational studies in the field of polaritonic chemistry. As two illustrative examples, we have optimized H_2O and H_2O_2 resonantly coupled to one or two cavity photon modes. For the case of H_2O , the predominant effect observed during the optimization processes is a rotation that leads to a reorientation of the molecule with respect to the photon modes. Surprisingly, we could even observe an effect of the restricted rotational degrees of freedom on the vibro-polaritonic IR spectrum for larger coupling strengths. These results clearly show that rotational motion is no longer an unrestricted degree of freedom in a cavity molecular system that can be neglected. In contrast, for the optimization of H_2O_2 , no rotational motion occurred for the chosen initial condi-

tions (orientation of the molecule and polarization axes of the cavity), and geometric relaxation is more important. Consequently, the interpretation of computational studies based on fixed molecular structures and fixed orientation should be viewed with caution. Comparing the optimizations of H_2O_2 coupled to one- and two-cavity modes, we want to highlight that the results have some similarities, but also show significant differences. The more realistic two-mode case with two cavity modes predicts smaller changes in the molecular structure, while the single-mode case overemphasizes them, even leading to a planar structure of H_2O_2 .

In agreement with recent studies [31, 37], we can confirm the minimization of the DSE contribution as the driving force for both orientation and geometrical relaxation. The DSE has been shown [31, 38–40] to be strictly necessary to obtain a finite polarization and a bounded solution. However, despite its importance, DSE is still a rather abstract idea, so we derived a more accessible concept to estimate the effect of cavity interaction on molecular geometry. We are able to explain the observed rotation of the cavity-coupled molecule by determining the main components of the polarizability tensor α . Without fixing its orientation, the molecule will reorient so that the cavity mode polarization axes align with the smallest components of the polarizability. With respect to geometric relaxation, we observed two effects: First, it aims to reduce the polarizability of the molecule and, second, it also reduces the dipole moment itself. The evaluation of both the dipole moment and the polarizability is likely to be a useful and simple tool to evaluate the possibility of influencing molecules and chemical reactions by strong light-matter interaction inside an optical cavity. Exploring the changes in orientation and geometries in molecular ensembles are a logical next step.

IV. METHODS

A. Theoretical background

Starting from the non-relativistic Pauli-Fierz Hamiltonian in the length gauge representation [41–45] we apply the cavity Born-Oppenheimer approximation (CBOA) [46–49] to simulate molecules interacting with the confined electromagnetic field in an optical cavity under VSC conditions. By making use of a generalized Born-Huang expansion [45, 50] the cavity modes are grouped with the nuclei and the resulting electronic subsystem can be solved in an *ab-initio* manner [31, 33, 51]. Atomic units ($\hbar = 4\pi\epsilon_0 = m_e = 1$) are used in the following unless otherwise noted, and bold symbols denote vectors. The electronic CBOA Hamiltonian for multiple cavity modes takes the form of

$$\hat{H}_{CBO} = \hat{H}_{el} + \sum_m^{N_M} \frac{1}{2} \omega_m^2 q_m^2 - \omega_m q_m (\boldsymbol{\lambda}_m \cdot \hat{\boldsymbol{\mu}}) + \frac{1}{2} (\boldsymbol{\lambda}_m \cdot \hat{\boldsymbol{\mu}})^2, \quad (1)$$

where $\hat{\boldsymbol{\mu}}$ represents the molecular dipole operator, which is defined by the operators of the N_{el} electron coordinates $\hat{\boldsymbol{r}}$ and the classic coordinates \mathbf{R} of the N_{Nuc} nuclei. \hat{H}_{el} is the Hamiltonian for the field-free many-electron system. Each of the N_m cavity modes contributes three additional terms to the electronic Hamiltonian. The first term is a harmonic potential introduced by the photon displacement field, with the classic photon displacement coordinate q_m and ω_m being the frequency of the cavity mode. The second term describes the dipole coupling between the molecular system and the photon displacement field, which is characterized by the coupling strength λ_m . The last term is the DSE operator [38–40], which is an energy contribution that describes the self-polarization of the molecule-cavity system. The cavity mode-specific coupling parameter λ_m for a cavity with effective mode volume V_m is defined as follows:

$$\lambda_m = e_m \lambda_m = e_m \sqrt{\frac{4\pi}{V_m}}. \quad (2)$$

The unit vector e_m denotes the polarization axis of the cavity mode m .

The many-electron problem described by Eq. 1 can be solved using the CBO-HF approach [31]. The resulting energy E_{CBO} is a function of the nuclear coordinates \mathbf{R} and the photon displacement coordinates \mathbf{q} , represented as a vector grouping all q_m :

$$E_{CBO} = \langle E_{CBO} \rangle(\mathbf{R}, \mathbf{q}) = \langle E_{el} \rangle(\mathbf{R}) + \sum_m^{N_M} \langle E_{lin}^{(m)} \rangle(\mathbf{R}, q_m) + \langle E_{dse}^{(m)} \rangle(\mathbf{R}) + E_{dis}^{(m)}(q_m) \quad (3)$$

The first derivative of the energy E_{CBO} with respect to the nuclear and photon displacement coordinates can be calculated analytically [35] and defines the CBO-HF gradient \mathbf{g}_{CBO} as a $(3N_A + N_M)$ vector, where N_A is the number of atoms in the molecule.

$$\mathbf{g} = \nabla E_{CBO} \quad (4)$$

Based on the analytic gradients, the CBO-Hessian matrix \mathbf{H} of size $(3N_A + N_M)(3N_A + N_M)$ is accessible via finite differences [35].

$$\mathbf{H}_{ij} = \nabla_i \mathbf{g}_j \approx \frac{\mathbf{g}_j(x_i + \Delta) - \mathbf{g}_j(x_i - \Delta)}{2\Delta} \quad (5)$$

with x_i being a nuclear or displacement coordinate. The molecular polarizability tensor α at the CBO-HF level is calculated as the first derivative of the CBO-HF dipole moment vector with respect to a small external field, also using finite differences. Both the analytic gradient and the numerical Hessian can be used to optimize molecules coupled to cavity photon modes. In this manuscript we use the Broyden–Fletcher–Goldfarb–Shanno (BFGS) algorithm:

$$\mathbf{x}_{n+1} = \mathbf{x}_n - \tilde{\mathbf{H}}^{-1} \mathbf{g}_{CBO}, \quad (6)$$

where \mathbf{x} is the combined nuclear and displacement coordinate vector $(3N_A + N_M)$ and \mathbf{g}_{CBO} the gradient vector. The approximate Hessian matrix $\tilde{\mathbf{H}}$ at each point n is updated with the Hessian matrix at stage $n - 1$ according to:

$$\tilde{\mathbf{H}}_n = \tilde{\mathbf{H}}_{n-1} + \frac{\Delta \mathbf{g} \cdot \Delta \mathbf{g}^T}{\Delta \mathbf{g}^T \cdot \Delta \mathbf{x}} - \frac{\tilde{\mathbf{H}}_{n-1} \cdot \Delta \mathbf{x} \cdot \Delta \mathbf{x}^T \tilde{\mathbf{H}}_{n-1}}{\Delta \mathbf{x}^T \cdot \tilde{\mathbf{H}}_{n-1} \cdot \Delta \mathbf{x}} \quad (7)$$

A detailed benchmark of the implemented BFGS algorithm against the Steepest Descent method and the Newton–Raphson method can be found in the Supporting Information.

B. Computational details

The BFGS algorithm, the necessary analytical gradients and the numerical Hessian for the CBO-HF ansatz have been implemented in the Psi4NumPy environment [52], which is an extension of the PSI4 [53] electronic structure package. All calculations were performed using the aug-cc-pVDZ basis set [54] and all geometries were pre-optimized at the Hartree-Fock level of theory. In all CBO-HF calculations performed in this work, we consider a lossless cavity. The coupling strength λ_m is chosen between 0.015 au and 0.150 au to assess the medium and strong coupling situation in the case of a single molecule. We emphasize that parts of the light-matter coupling used here are significantly larger than what can presently be achieved in experiments. For example, $\lambda_m = 0.1$ au corresponds to an effective mode volume of less than 0.2 nm^3 , which is less than the typical mode volumes of approximately 10.0 nm^3 that can be achieved in plasmonic cavities [1, 55].

The CBO-HF energy and gradients depend on the relative orientation of the molecule and the polarization axes of the cavity. For this reason, the internal coordinate system traditionally used to optimize molecular geometries is a poor choice because it neglects spatial orientation. Therefore, all geometry optimizations in this work were performed using Cartesian coordinates. For the first step of the BFGS optimization, the exact Hessian matrix was computed, and to improve convergence for the H_2O optimization, the exact Hessian was recomputed after every 10th step. The maximum component and the root mean square deviation of the gradient and the displacement vector are used as convergence criteria. For the gradient, both must be less than 10^{-5} au and for the displacement vector, both must be less than 10^{-4} au. The semiclassical harmonic approximation [35] was used to determine the normal modes and frequencies of the optimized coupled cavity-molecular systems. All optimized structures discussed in this manuscript are real minima, since they have no imaginary frequencies.

ACKNOWLEDGMENTS

M.K. acknowledges funding from the European Union’s Horizon 2020 research. This project has received funding from the European Research Council (ERC) under the European Union’s Horizon 2020 research and innovation program (grant agreement no. 852286).

AUTHOR CONTRIBUTIONS

T.S. and M.K. designed the research. T.S. implemented the optimization routines and performed the simulations. T.S. and M.K. contributed equally on analyzing

the data and writing the manuscript.

COMPETING INTERESTS

The authors declare no competing interests.

SUPPLEMENTARY INFORMATION

The supplementary material includes a detailed analysis of vibro-polaritonic normal modes, a benchmark optimization method and parameters, and all optimized geometries. Correspondence and requests for materials should be addressed to T.S. or M.K.

-
- [1] Benz, F. *et al.* Single-molecule optomechanics in “picocavities”. *Science* **354**, 726–729 (2016).
- [2] Griffiths, J., de Nijs, B., Chikkaraddy, R. & Baumberg, J. J. Locating Single-Atom optical picocavities using Wavelength-Multiplexed raman scattering. *ACS Photonics* **8**, 2868–2875 (2021).
- [3] Basov, D. N., Asenjo-Garcia, A., James Schuck, P., Zhu, X. & Rubio, A. Polariton panorama. *Nanophotonics* **10**, 549–577 (2021).
- [4] Ribeiro, R. F., Martínez-Martínez, L. A., Du, M., Campos-Gonzalez-Angulo, J. & Yuen-Zhou, J. Polariton chemistry: controlling molecular dynamics with optical cavities. *Chem. Sci.* **9**, 6325–6339 (2018).
- [5] Ebbesen, T. W., Rubio, A. & Scholes, G. D. Introduction: Polaritonic chemistry. *Chem. Rev.* **123**, 12037–12038 (2023).
- [6] Bhuyan, R. *et al.* The rise and current status of polaritonic photochemistry and photophysics. *Chem. Rev.* (2023).
- [7] Hutchison, J. A., Schwartz, T., Genet, C., Devaux, E. & Ebbesen, T. W. Modifying chemical landscapes by coupling to vacuum fields. *Angew. Chem. Int. Ed Engl.* **51**, 1592–1596 (2012).
- [8] Thomas, A. *et al.* Tilting a ground-state reactivity landscape by vibrational strong coupling. *Science* **363**, 615–619 (2019).
- [9] Sau, A. *et al.* Modifying Woodward-Hoffmann stereoselectivity under vibrational strong coupling. *Angew. Chem. Int. Ed Engl.* **60**, 5712–5717 (2021).
- [10] Fukushima, T., Yoshimitsu, S. & Murakoshi, K. Inherent promotion of ionic conductivity via collective vibrational strong coupling of water with the vacuum electromagnetic field. *J. Am. Chem. Soc.* **144**, 12177–12183 (2022).
- [11] Vergauwe, R. M. A. *et al.* Modification of enzyme activity by vibrational strong coupling of water. *Angew. Chem. Int. Ed Engl.* **58**, 15324–15328 (2019).
- [12] Bai, J. *et al.* Vibrational coupling with O-H stretching increases catalytic efficiency of sucrase in Fabry-Pérot microcavity. *Biochem. Biophys. Res. Commun.* **652**, 31–34 (2023).
- [13] Felicetti, S. *et al.* Photoprotecting uracil by coupling with lossy nanocavities. *J. Phys. Chem. Lett.* **11**, 8810–8818 (2020).
- [14] Campos-Gonzalez-Angulo, J. A. & Yuen-Zhou, J. Polaritonic normal modes in transition state theory. *J. Chem. Phys.* **152**, 161101 (2020).
- [15] Li, X., Mandal, A. & Huo, P. Cavity frequency-dependent theory for vibrational polariton chemistry. *Nat. Commun.* **12**, 1315 (2021).
- [16] Galego, J., Climent, C., Garcia-Vidal, F. J. & Feist, J. Cavity Casimir-Polder forces and their effects in Ground-State chemical reactivity. *Phys. Rev. X* **9**, 021057 (2019).
- [17] Schäfer, C., Flick, J., Ronca, E., Narang, P. & Rubio, A. Shining light on the microscopic resonant mechanism responsible for cavity-mediated chemical reactivity. *Nat. Commun.* **13**, 7817 (2022).
- [18] Li, T. E., Nitzan, A. & Subotnik, J. E. On the origin of ground-state vacuum-field catalysis: Equilibrium consideration. *J. Chem. Phys.* **152**, 234107 (2020).
- [19] Pavošević, F., Smith, R. L. & Rubio, A. Cavity click chemistry: Cavity-Catalyzed Azide-Alkyne cycloaddition. *J. Phys. Chem. A* **127**, 10184–10188 (2023).
- [20] Pavošević, F., Smith, R. L. & Rubio, A. Computational study on the catalytic control of endo/exo Diels-Alder reactions by cavity quantum vacuum fluctuations. *Nat. Commun.* **14**, 2766 (2023).
- [21] Vidal, M. L., Manby, F. R. & Knowles, P. J. Polaritonic effects in the vibronic spectrum of molecules in an optical cavity. *J. Chem. Phys.* **156**, 204119 (2022).
- [22] Riso, R. R., Haugland, T. S., Ronca, E. & Koch, H. On the characteristic features of ionization in QED environments. *J. Chem. Phys.* **156**, 234103 (2022).
- [23] Severi, M. & Zerbetto, F. Polaritonic chemistry: Hindering and easing ground state polyenic isomerization via breakdown of σ - π separation. *J. Phys. Chem. Lett.* 9145–9149 (2023).
- [24] Vu, N., McLeod, G. M., Hanson, K. & DePrince, A. E., Iii. Enhanced diastereocontrol via strong Light-Matter interactions in an optical cavity. *J. Phys. Chem. A* (2022).
- [25] Pavošević, F., Hammes-Schiffer, S., Rubio, A. & Flick, J. Cavity-Modulated proton transfer reactions. *J. Am. Chem. Soc.* **144**, 4995–5002 (2022).
- [26] Tokatly, I. V. Time-dependent density functional theory for many-electron systems interacting with cavity photons. *Phys. Rev. Lett.* **110**, 233001 (2013).

- [27] Ruggenthaler, M. *et al.* Quantum-electrodynamical density-functional theory: Bridging quantum optics and electronic-structure theory. *Phys. Rev. A* **90**, 012508 (2014).
- [28] Flick, J., Appel, H., Ruggenthaler, M. & Rubio, A. Cavity Born-Oppenheimer approximation for correlated Electron-Nuclear-Photon systems. *J. Chem. Theory Comput.* **13**, 1616–1625 (2017).
- [29] Haugland, T. S., Ronca, E., Kjønstad, E. F., Rubio, A. & Koch, H. Coupled cluster theory for molecular polaritons: Changing ground and excited states. *Phys. Rev. X* **10**, 041043 (2020).
- [30] McTague, J. & Foley, J. J., 4th. Non-Hermitian cavity quantum electrodynamics-configuration interaction singles approach for polaritonic structure with ab initio molecular hamiltonians. *J. Chem. Phys.* **156**, 154103 (2022).
- [31] Schnappinger, T., Sidler, D., Ruggenthaler, M., Rubio, A. & Kowalewski, M. Cavity Born-Oppenheimer Hartree-Fock ansatz: Light-Matter properties of strongly coupled molecular ensembles. *J. Phys. Chem. Lett.* **14**, 8024–8033 (2023).
- [32] Foley, J. J., McTague, J. F. & DePrince, A. E. Ab initio methods for polariton chemistry. *Chem. Phys. Rev.* **4** (2023).
- [33] Angelico, S., Haugland, T. S., Ronca, E. & Koch, H. Coupled cluster cavity Born-Oppenheimer approximation for electronic strong coupling. *J. Chem. Phys.* **159** (2023).
- [34] Liebenthal, M. D., Vu, N. & DePrince, A. E., 3rd. Assessing the effects of orbital relaxation and the Coherent-State transformation in quantum electrodynamics density functional and Coupled-Cluster theories. *J. Phys. Chem. A* (2023).
- [35] Schnappinger, T. & Kowalewski, M. Ab initio Vibro-Polaritonic spectra in strongly coupled Cavity-Molecule systems. *J. Chem. Theory Comput.* **19**, 9278–9289 (2023).
- [36] Sidler, D. *et al.* Unraveling a Cavity-Induced molecular polarization mechanism from collective vibrational strong coupling. *J. Phys. Chem. Lett.* 5208–5214 (2024).
- [37] Liebenthal, M. D. & Eugene DePrince, A., III. The orientation dependence of cavity-modified chemistry (2024). 2405.01676.
- [38] Rokaj, V., Welakuh, D. M., Ruggenthaler, M. & Rubio, A. Light-matter interaction in the long-wavelength limit: no ground-state without dipole self-energy. *J. Phys. B At. Mol. Opt. Phys.* **51**, 034005 (2018).
- [39] Schäfer, C., Ruggenthaler, M., Rokaj, V. & Rubio, A. Relevance of the quadratic diamagnetic and Self-Polarization terms in cavity quantum electrodynamics. *ACS Photonics* **7**, 975–990 (2020).
- [40] Sidler, D., Ruggenthaler, M., Schäfer, C., Ronca, E. & Rubio, A. A perspective on ab initio modeling of polaritonic chemistry: The role of non-equilibrium effects and quantum collectivity. *J. Chem. Phys.* **156**, 230901 (2022).
- [41] Spohn, H. *Dynamics of charged particles and their radiation field* (Cambridge university press, 2004).
- [42] Ruggenthaler, M., Tancogne-Dejean, N., Flick, J., Appel, H. & Rubio, A. From a quantum-electrodynamical light-matter description to novel spectroscopies. *Nature Reviews Chemistry* **2**, 1–16 (2018).
- [43] Jestädt, R., Ruggenthaler, M., Oliveira, M. J., Rubio, A. & Appel, H. Light-matter interactions within the ehrenfest-maxwell-pauli-kohn-sham framework: fundamentals, implementation, and nano-optical applications. *Adv. Phys.* **68**, 225–333 (2019).
- [44] Lindoy, L. P., Mandal, A. & Reichman, D. R. Quantum dynamical effects of vibrational strong coupling in chemical reactivity. *Nature Communications* **14**, 2733 (2023).
- [45] Ruggenthaler, M., Sidler, D. & Rubio, A. Understanding polaritonic chemistry from ab initio quantum electrodynamics. *Chem. Rev.* **123**, 11191–11229 (2023).
- [46] Flick, J., Ruggenthaler, M., Appel, H. & Rubio, A. Atoms and molecules in cavities, from weak to strong coupling in quantum-electrodynamics (qed) chemistry. *Proc. Natl. Acad. Sci. U.S.A.* **114**, 3026–3034 (2017).
- [47] Flick, J., Appel, H., Ruggenthaler, M. & Rubio, A. Cavity born-oppenheimer approximation for correlated electron-nuclear-photon systems. *J. Chem. Theory Comput.* **13**, 1616–1625 (2017).
- [48] Flick, J. & Narang, P. Cavity-Correlated Electron-Nuclear dynamics from first principles. *Phys. Rev. Lett.* **121**, 113002 (2018).
- [49] Fischer, E. W. & Saalfrank, P. Beyond cavity Born-Oppenheimer: On nonadiabatic coupling and effective ground state hamiltonians in Vibro-Polaritonic chemistry. *J. Chem. Theory Comput.* **19**, 7215–7229 (2023).
- [50] Schäfer, C., Ruggenthaler, M. & Rubio, A. Ab initio non-relativistic quantum electrodynamics: Bridging quantum chemistry and quantum optics from weak to strong coupling. *Phys. Rev. A* **98**, 043801 (2018).
- [51] Sidler, D. *et al.* Unraveling a Cavity-Induced molecular polarization mechanism from collective vibrational strong coupling. *J. Phys. Chem. Lett.* **15**, 5208–5214 (2024).
- [52] Smith, D. G. A. *et al.* Psi4NumPy: An interactive quantum chemistry programming environment for reference implementations and rapid development. *J. Chem. Theory Comput.* **14**, 3504–3511 (2018).
- [53] Smith, D. G. A. *et al.* Psi4 1.4: Open-source software for high-throughput quantum chemistry. *J. Chem. Phys.* **152**, 184108 (2020).
- [54] Kendall, R. A., Dunning, T. H. & Harrison, R. J. Electron affinities of the first-row atoms revisited. systematic basis sets and wave functions. *J. Chem. Phys.* **96**, 6796–6806 (1992).
- [55] Mondal, M., Semenov, A., Ochoa, M. A. & Nitzan, A. Strong coupling in infrared plasmonic cavities. *J. Phys. Chem. Lett.* **13**, 9673–9678 (2022).

Supporting Information:

Do Molecular Geometries Change Under Vibrational Strong Coupling?

Thomas Schnappinger* and Markus Kowalewski*

*Department of Physics, Stockholm University, AlbaNova University Center, SE-106 91
Stockholm, Sweden*

E-mail: thomas.schnappinger@fysik.su.se; markus.kowalewski@fysik.su.se

Contents

S1 Vibro-Polaritonic Normal Modes Analysis	2
S2 Benchmark Optimization Methods and Parameters	5
S3 Optimized geometries	10
S3.1 Optimized H ₂ O coupled to a single cavity mode	10
S3.2 Optimized H ₂ O coupled to two orthogonal cavity modes	12
S3.3 Optimized H ₂ O ₂ coupled to a single cavity mode	14
S3.4 Optimized H ₂ O ₂ coupled to two orthogonal cavity modes	16
References	18

S1 Vibro-Polaritonic Normal Modes Analysis

The general concept of performing a normal mode analysis in the cavity Born-Oppenheimer approximation (CBOA) was introduced in our previous work,¹ and the reader is referred to the paper for details of the theory. For convenience, the main ideas are summarized in the following. The harmonic approximation gives access to the normal modes \mathbf{a}_i . In CBOA the normal mode vectors have terms a_c describing the change in the classical photon displacement field coordinates q_m . The value of $|a_c|^2$ for a given normal mode is a measure of how strongly the corresponding vibrational transition interacts with the photon field. For an uncoupled light-matter system, a pure molecular transition is characterized by a $|a_c|^2$ value of zero, whereas the bare photon mode has a value of one. Note that due to the length gauge description q_m and the corresponding value a_c are no longer a pure photonic quantity if light and matter are coupled.²⁻⁴ However, $|a_c|^2$ can still be used as a probe to identify how photonic the corresponding vibrational transition is. The information obtained is comparable to the coefficients in the Hopfield models.⁵

In the following, we use the $|a_c|^2$ values to characterize all relevant transitions in the vibro-polaritonic IR spectra of all optimized structures. For the case of the coupled H₂O-cavity system, we also discuss the signal intensities \mathcal{I} in the harmonic approximation. The intensities are calculated as the projection of the dipole moment gradient on the normal mode vectors \mathbf{a}_i :

$$\mathcal{I}_i = (\nabla \langle \hat{\boldsymbol{\mu}} \rangle \cdot \mathbf{a}_i)^2 . \quad (\text{S1})$$

Fig. S1 shows the $|a_c|^2$ values and the harmonic intensities \mathcal{I} of the relevant transitions as a function of the coupling strength λ_m for optimized H₂O-cavity systems.

In the case of a single cavity mode coupled to H₂O, only three transitions are relevant to explain the spectral features in the vicinity of 1744 cm⁻¹. The main transition ν_2 shown as a green dashed line in Fig. S1 a) and b) corresponds to the molecular bending mode. It does not hybridize with the photon mode and its intensity is constant with increasing λ_m .

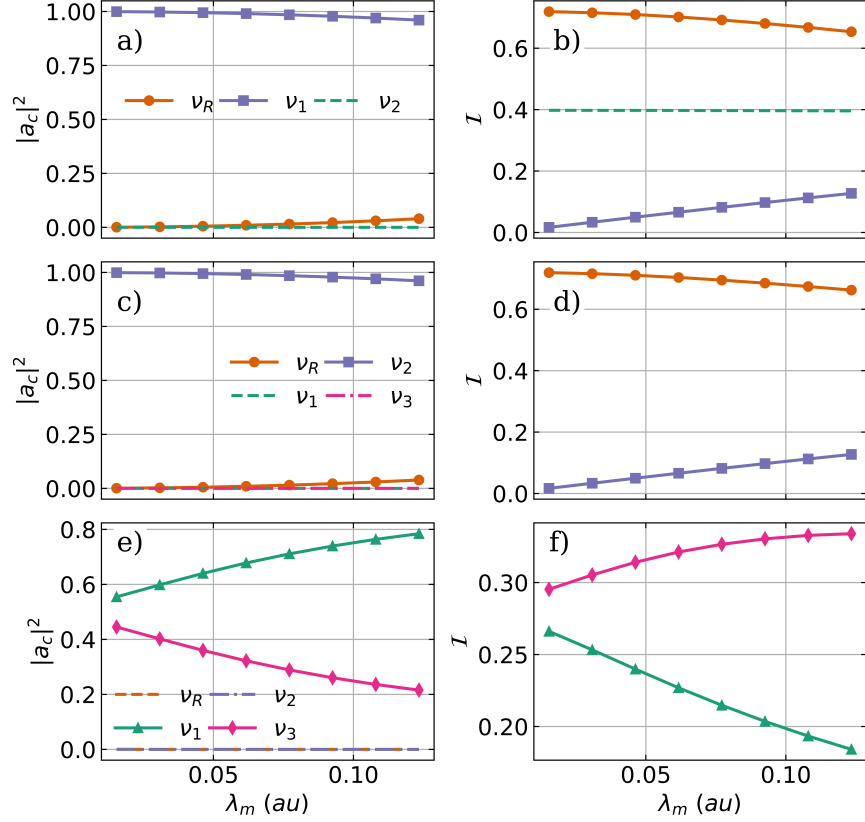


Figure S1: Relevant $|a_c|^2$ values and harmonic intensities \mathcal{I} as a function of the coupling strength λ_m for optimized H₂O structures coupled to a single cavity mode a) and b) as well as to two orthogonal cavity modes c), d), e) and f). The values for the cavity mode with the polarization axis \mathbf{e}_2 orthogonal to the dipole moment are given in c) and d) and for the one with the polarization axis \mathbf{e}_1 parallel to the dipole moment in e) and f). The cavity frequency ω_c is 1744 cm⁻¹ and the cavity coupling λ_m increases from 0.015 au to 0.123 au.

In contrast, ν_1 , shown as purple in Fig. S1 a) and b), is purely photonic at low coupling and has an intensity close to zero. With increasing coupling strength, ν_1 begins to weakly pair to a rotational mode (ν_R orange line). As a consequence, ν_R becomes slightly photonic and at the same time ν_1 gains intensity.

In the case of H₂O coupled to two orthogonal cavity modes, we divide the discussion into two parts: First, the photon mode orthogonal to the dipole moment shown in Fig. S1 c) and d) and second, the one parallel to the dipole mode shown in Fig. S1 e) and f). For the orthogonal cavity mode, the picture is almost identical to the single-mode case. The photon mode transition ν_2 starts almost decoupled and dark but starts to weakly couple to

the rotational mode transition ν_R with increasing coupling strength. In contrast, in the case of the parallel cavity mode, the transitions ν_1 and ν_3 are clearly hybridized already for low coupling strengths and stay so for increasing λ_m .

In Fig. S2 we show the $|a_c|^2$ values of the four relevant transitions for the optimized H_2O_2 molecule coupled to a single cavity mode as a function of the coupling strength λ_m . The asymmetric bending mode transition ν_4 (pink) and the cavity photon mode transition

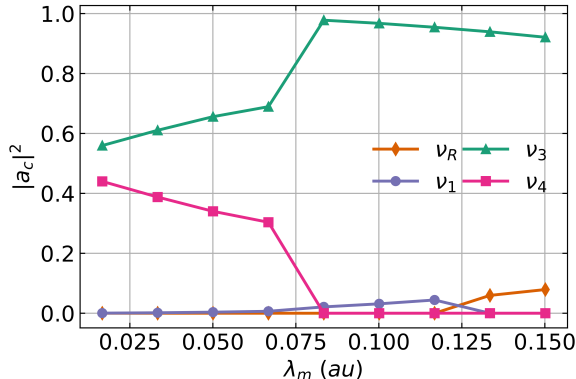


Figure S2: $|a_c|^2$ values of the four relevant transitions for the optimized H_2O_2 molecule coupled to a single cavity mode as a function of the coupling strength λ_m . The cavity frequency ω_c is 1491 cm^{-1} and the cavity coupling λ_m increases from 0.015 au to 0.150 au.

ν_3 (green) are clearly hybridized for low coupling strengths, smaller than 0.075 au. Due to geometrical changes, the cavity photon mode transition ν_3 decouples from ν_4 for larger λ_m and starts to interact weakly with the H_2O_2 twisting mode (ν_1 purple). For even higher coupling strengths and close to planarization, ν_3 is weakly coupled to a rotational mode (ν_R orange), similar to the H_2O case.

The $|a_c|^2$ values of the four relevant transitions for the optimized H_2O_2 molecule coupled to two orthogonal cavity modes are depicted in Fig. S3.

For the orthogonal cavity mode Fig. S3 a), the corresponding photon mode transition ν_4 (green) starts almost decoupled and dark, but starts to couple weakly to the H_2O_2 twisting mode (ν_1 orange) with increasing coupling strength. In contrast, in the case of the parallel cavity mode Fig. S3 b), the transitions ν_3 and ν_5 are clearly hybridized already at low coupling strengths and stay so for increasing λ_m .

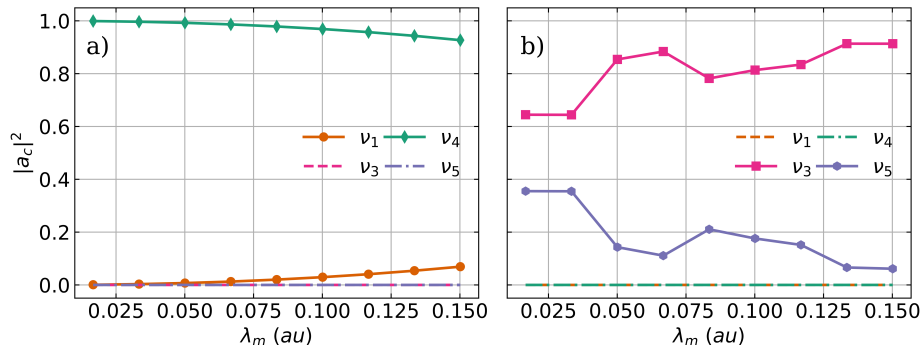


Figure S3: $|a_c|^2$ values of the four relevant transitions for the optimized H_2O_2 molecule coupled to two orthogonal cavity modes as a function of the coupling strength λ_m . a) For the cavity mode with the polarization axis \mathbf{e}_2 orthogonal to the dipole moment and b) for the one with the polarization axis \mathbf{e}_1 parallel to the dipole moment. The cavity frequency ω_c is 1491 cm^{-1} and the cavity coupling λ_m increases from 0.015 au to 0.150 au .

S2 Benchmark Optimization Methods and Parameters

We benchmark the performance of various algorithms for the optimization of coupled molecular-cavity systems in the CBOA representation. As a test case, we optimize a H_2O molecule coupled to a cavity. For the case of a single cavity mode, \mathbf{e} is neither parallel nor orthogonal to the molecular plane. In the case of two modes, \mathbf{e}_1 is in the molecular plane and \mathbf{e}_2 is aligned with the normal vector of the molecular plane. The simplest algorithm used is the Steepest Descent (SD) method, which requires only the gradient in each optimization step. The most computationally intensive is the Newton–Raphson (NR) method, which requires the exact Hessian matrix in each step. The Broyden–Fletcher–Goldfarb–Shanno (BFGS) algorithm offers a middle ground between SD and NR in terms of computational complexity. It uses an updating scheme that approximates the Hessian matrix at each point n using the gradient, the displacement, and the Hessian matrix at step $n - 1$. For the simplest version of the BFGS method, the identity matrix is used as an approximate Hessian at $n = 0$. To improve the performance, the exact Hessian can be used in the first step and during the optimization the exact Hessian can be recomputed after a certain number of steps. We have included an augmented Hessian method for each optimization routine in which we use the

exact Hessian to ensure that the Hessian matrix is positively defined.

$$\mathbf{x}_{n+1} = \mathbf{x}_n - (\mathbf{H} - (\min(\epsilon) + \gamma)\mathbf{1})^{-1} \mathbf{g}. \quad (\text{S2})$$

Here, $\min(\epsilon)$ is the smallest eigenvalue of the Hessian matrix and γ is a small number to prevent the augmented Hessian matrix from being non-invertible. The augmentation is necessary to avoid inadvertently optimizing a transition state or a higher-order saddle point.

Fig. S4 shows the convergence behavior for different optimization algorithms.

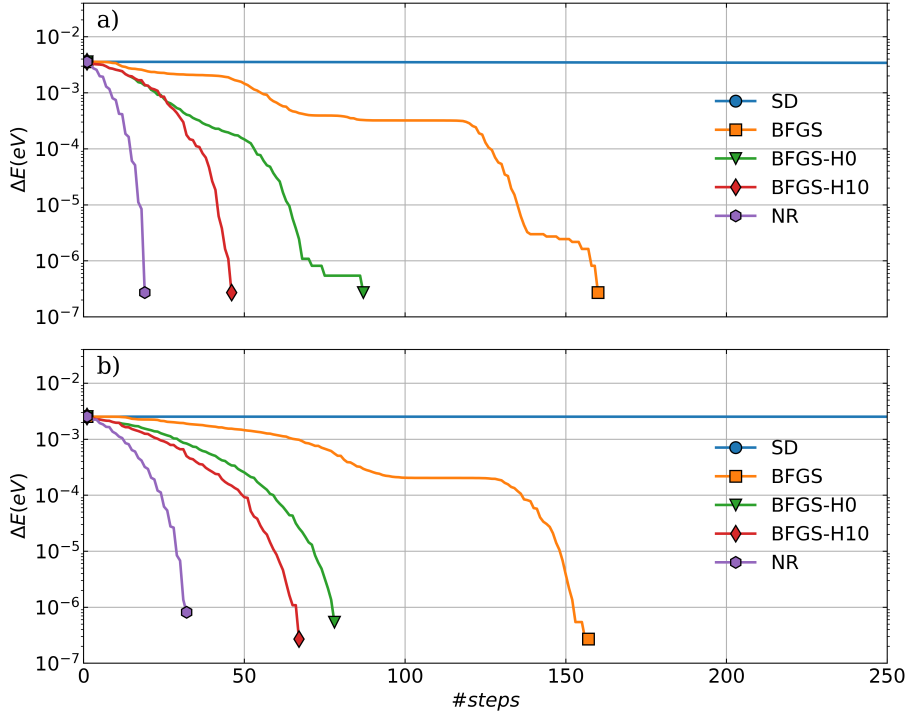


Figure S4: Energy convergence for the optimization of a single H_2O molecule coupled to a) one cavity photon mode or b) two cavity photon modes for $\omega_m = 1744.0 \text{ cm}^{-1}$ and $\lambda_m = 0.031 \text{ au}$ using different optimization routines. The different optimization routines are color-coded. The different versions of the BFGS method are labeled as follows: BFGS started with the identity matrix and no Hessian was computed, BFGS-H0 started with the exact Hessian, and BFGS-H10 started with the exact Hessian and recomputed it every 10th step. The starting point and the converged end point are marked.

The SD method does not converge within the maximum number of 250 steps. The NR method and all versions of the BFGS method converge to the same minimum structure. As

expected, the NR method shows the fastest convergence, while the simplest BFGS version needs about three times more optimization steps. Including Hessian information in the BFGS algorithm significantly speeds up convergence, especially when the exact Hessian is recomputed during optimization. In Fig. S5 the energy convergence for different intervals for the reactivation of the Hessian is shown.

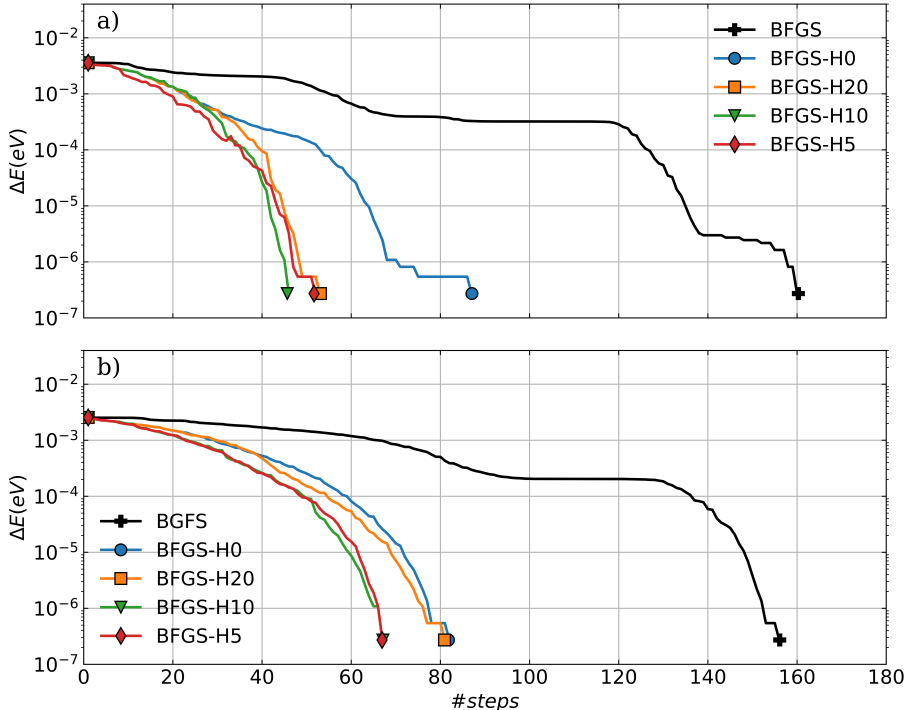


Figure S5: Energy convergence for the optimization of a single H_2O molecule coupled to a) one cavity photon mode or b) two cavity photon modes for $\omega_m = 1744.0 \text{ cm}^{-1}$ and $\lambda_m = 0.031 \text{ au}$ using different versions of the BFGS routine. Different intervals for recalculation of the exact Hessian are color-coded. The BFGS results without the exact Hessian are shown in black. The starting point and the converged end point are marked.

For the case of H_2O coupled to a single cavity mode (Fig. S6 a)), recalculating the exact Hessian during optimization significantly speeds up convergence. However, changing the interval from every 20th step to every 5th step shows only a small improvement. This finding also holds for the case of two orthogonal cavity modes, shown in Fig. S6 b).

To improve convergence and overall stability, we implement a trust-radius approach combined with a backtracking line search in our optimization routines. The trust-radius approach

sets an upper bound R for the step size, while the backtracking line search further reduces the step size if the energy increases along the step. The latter comes with a cost of additional single-point calculations during each optimization step. The energy convergence for different trust radii R is shown in Fig. S6 and for different number of iterations of the backtracking line search is shown in Fig. S7.

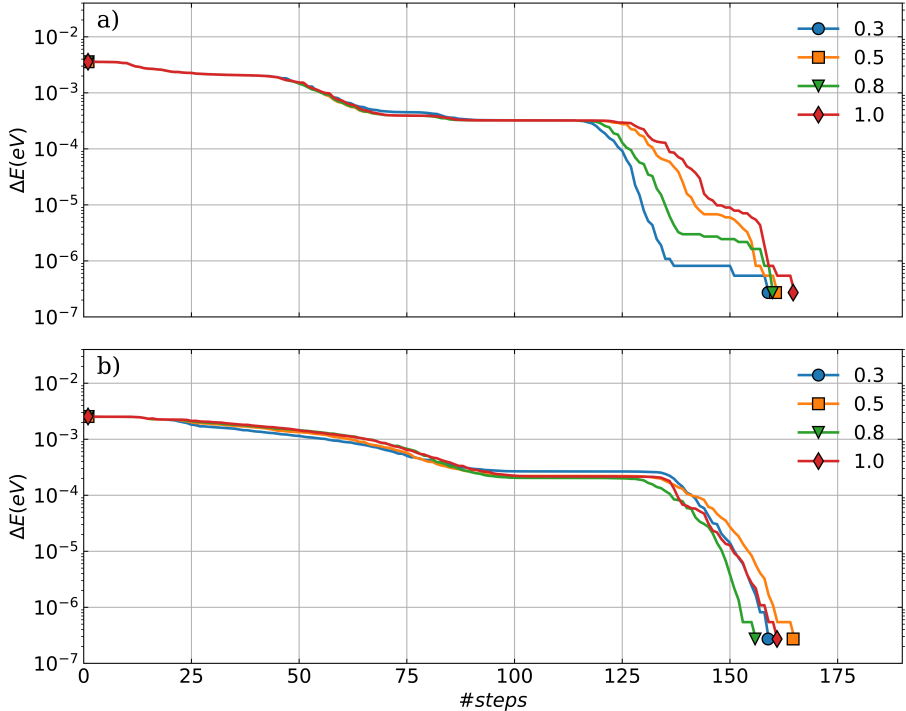


Figure S6: Energy convergence for the optimization of a single H_2O molecule coupled to a) one cavity photon mode or b) two cavity photon modes for $\omega_m = 1744.0 \text{ cm}^{-1}$ and $\lambda_m = 0.031 \text{ au}$ using the BFGS routine recalculating the Hessian in every 10th step and 5 steps in the backtracking line search. Different values for the trust radius R are color-coded. The starting point and the converged end point are marked.

The chosen size of the trust radius R has only a small influence on convergence, and a value of 0.8 au shows the best results (green line in Fig. S6). In contrast, the number of iterations of the backtracking line search has an impact on both stability and convergence. With more steps in the line search, the average step size is getting smaller, and therefore more steps are needed. However, without line search (blue line in Fig. S7), the energy change is highly fluctuating, making optimization more unstable. The best results in both stability

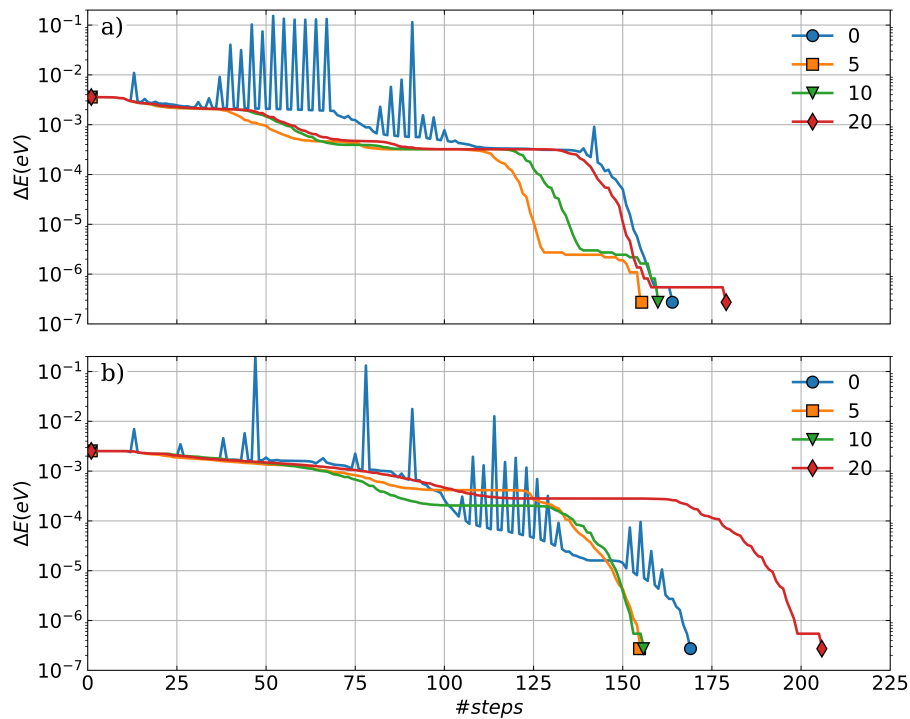


Figure S7: Energy convergence for the optimization of a single H₂O molecule coupled to a) one cavity photon mode or b) two cavity photon modes for $\omega_m = 1744.0 \text{ cm}^{-1}$ and $\lambda_m = 0.031 \text{ au}$ using the BFGS routine recalculating the Hessian in every 10th step and a trust radius of 0.8 au. Different numbers of steps in the backtracking line search are color-coded. The starting point and the converged end point are marked.

and convergence are achieved for 5 steps in the backtracking line search (orange line in Fig. S7)

S3 Optimized geometries

S3.1 Optimized H₂O coupled to a single cavity mode

All optimizations were performed using the BFGS method, starting from the exact Hessian matrix in the first step and recalculating it after every 10th step. The minima found were verified to have no imaginary frequency.

Table 1: $\lambda_m = 0.015$ au and $q_1 = 0.0000$ au.

O	0.0000	-0.0282	-0.1101
H	0.0000	-0.6170	0.6273
H	0.0000	0.8425	0.2536

Table 2: $\lambda_m = 0.031$ au and $q_1 = 0.0000$ au.

O	0.0000	-0.0260	-0.1107
H	0.0000	-0.6294	0.6146
H	0.0000	0.8370	-0.2707

Table 3: $\lambda_m = 0.046$ au and $q_1 = 0.0000$ au.

O	0.0000	-0.0252	-0.1108
H	0.0000	-0.6335	0.6107
H	0.0000	0.8349	0.2766

Table 4: $\lambda_m = 0.062$ au and $q_1 = 0.0000$ au.

O	0.0000	-0.0070	-0.1134
H	0.0000	-0.7233	0.5000
H	0.0000	0.7791	0.4075

Table 5: $\lambda_m = 0.077$ au and $q_1 = 0.0000$ au.

O	0.0000	-0.2666	-0.1105
H	0.0000	-0.6247	0.6182
H	0.0000	0.8379	0.2655

Table 6: $\lambda_m = 0.093$ au and $q_1 = 0.0000$ au.

O	0.0000	-0.0036	0.1136
H	0.0000	-0.7372	-0.4779
H	0.0000	0.7658	-0.4305

Table 7: $\lambda_m = 0.101$ au and $q_1 = 0.0000$ au.

O	0.0000	0.0099	0.1132
H	0.0000	-0.7880	-0.3874
H	0.0000	0.7091	-0.5179

Table 8: $\lambda_m = 0.123$ au and $q_1 = 0.0000$ au.

O	0.0000	0.0027	-0.1135
H	0.0000	-0.7614	0.4363
H	0.0000	0.7398	0.4720

S3.2 Optimized H₂O coupled to two orthogonal cavity modes

All optimizations were performed using the BFGS method, starting from the exact Hessian matrix in the first step and recalculating it after every 10th step. The minima found were verified to have no imaginary frequency.

Table 9: $\lambda_m = 0.015$ au, $q_1 = -1.5005$ au and $q_2 = 0.0000$ au.

O	-0.1136	0.0000	0.0000
H	0.4542	0.0000	0.7535
H	0.4542	0.0000	-0.7535

Table 10: $\lambda_m = 0.031$ au, $q_1 = -3.0012$ au and $q_2 = 0.0000$ au.

O	-0.1135	0.0000	0.0000
H	0.4536	0.0000	0.7535
H	0.4536	0.0000	-0.7535

Table 11: $\lambda_m = 0.046$ au, $q_1 = -4.5021$ au and $q_2 = 0.0000$ au.

O	-0.1132	0.0000	0.0000
H	0.4526	0.0000	0.7536
H	0.4526	0.0000	-0.7536

Table 12: $\lambda_m = 0.062$ au, $q_1 = -6.0033$ au and $q_2 = 0.0000$ au.

O	-0.1129	0.0000	0.0000
H	0.4513	0.0000	0.7537
H	0.4513	0.0000	-0.7537

Table 13: $\lambda_m = 0.077$ au, $q_1 = -7.5050$ au and $q_2 = 0.0000$ au.

O	-0.1125	0.0000	0.0000
H	0.4497	0.0000	0.7538
H	0.4497	0.0000	-0.7538

Table 14: $\lambda_m = 0.093$ au, $q_1 = -9.0068$ au and $q_2 = 0.0000$ au.

O	-0.1120	0.0000	0.0000
H	0.4480	0.0000	0.7538
H	0.4480	0.0000	-0.7538

Table 15: $\lambda_m = 0.101$ au, $q_1 = -10.5084$ au and $q_2 = 0.0000$ au.

O	-0.1114	0.0000	0.0000
H	0.4453	0.0000	0.7542
H	0.4460	0.0000	-0.7542

Table 16: $\lambda_m = 0.123$ au, $q_1 = -12.0095$ au and $q_2 = 0.0000$ au.

O	-0.1108	0.0000	0.0000
H	0.4430	0.0000	0.7543
H	0.4430	0.0000	-0.7543

S3.3 Optimized H₂O₂ coupled to a single cavity mode

All optimizations were performed using the BFGS method, starting from the exact Hessian matrix in the first step. The minima found were verified to have no imaginary frequency.

Table 17: $\lambda_m = 0.017$ au and $q_1 = 1.8231$ au.

O	-0.1693	-0.6737	0.0575
H	0.5197	-1.0623	-0.4600
O	0.1693	0.6737	0.0575
H	-0.5197	1.0623	-0.4600

Table 18: $\lambda_m = 0.033$ au and $q_1 = 3.5933$ au.

O	-0.1066	-0.6864	0.0566
H	0.6204	-1.0101	-0.4529
O	0.1066	0.6864	0.0566
H	-0.6204	1.0101	-0.4529

Table 19: $\lambda_m = 0.050$ au and $q_1 = 5.2569$ au.

O	-0.1731	-0.6727	0.0551
H	0.5276	-1.0669	-0.4406
O	0.1731	0.6727	0.0551
H	-0.5276	1.0669	-0.4406

Table 20: $\lambda_m = 0.067$ au and $q_1 = 6.7444$ au.

O	-0.1766	-0.6719	0.0529
H	0.5342	-1.0711	-0.4229
O	0.1766	0.6719	0.0529
H	-0.5342	1.0711	-0.4229

Table 21: $\lambda_m = 0.083$ au and $q_1 = 8.7840$ au.

O	-0.1869	-0.6693	0.0456
H	0.5535	-1.0840	-0.3644
O	0.1869	0.6693	0.0456
H	-0.5535	1.0840	-0.3644

Table 22: $\lambda_m = 0.100$ au and $q_1 = 8.9450$ au.

O	-0.1944	-0.6675	0.0396
H	0.5662	-1.0934	-0.3169
O	0.1944	0.6675	0.0396
H	-0.5662	1.0934	-0.3169

Table 23: $\lambda_m = 0.117$ au and $q_1 = 7.7993$ au.

O	-0.2030	-0.6656	0.0301
H	0.5841	-1.1051	-0.2407
O	0.2030	0.6656	0.0301
H	-0.5841	1.1051	-0.2407

Table 24: $\lambda_m = 0.133$ au and $q_1 = 0.0007$ au.

O	-0.2124	-0.6638	0.0251
H	0.6112	-1.1193	-0.1507
O	0.2124	0.6638	0.0251
H	-0.6112	1.1193	-0.1507

Table 25: $\lambda_m = 0.150$ au and $q_1 = 0.0000$ au.

O	-0.2130	-0.6631	0.0000
H	0.6097	-1.1189	0.0000
O	0.2130	0.6097	0.0000
H	-0.5197	1.1189	0.0000

S3.4 Optimized H₂O₂ coupled to two orthogonal cavity modes

All optimizations were performed using the BFGS method, starting from the exact Hessian matrix in the first step. The minima found were verified to have no imaginary frequency.

Table 26: $\lambda_m = 0.017$ au, $q_1 = 1.8296$ au and $q_2 = 0.0000$ au.

O	-0.2056	-0.6635	0.0577
H	0.4597	-1.0887	-0.4618
O	0.2056	0.6635	0.0577
H	-0.4597	1.0887	-0.4618

Table 27: $\lambda_m = 0.033$ au, $q_1 = 3.6526$ au and $q_2 = 0.0000$ au.

O	-0.2060	-0.6630	0.0575
H	0.4591	-1.0894	-0.4602
O	0.2060	0.6630	0.0575
H	-0.4591	1.0894	-0.4602

Table 28: $\lambda_m = 0.050$ au, $q_1 = 5.4627$ au and $q_2 = 0.0000$ au.

O	-0.2067	-0.6623	0.0572
H	0.4581	-1.0904	-0.4575
O	0.2067	0.6623	0.0572
H	-0.4581	1.0904	-0.4575

Table 29: $\lambda_m = 0.067$ au, $q_1 = 7.2555$ au and $q_2 = 0.0000$ au.

O	-0.2076	-0.6612	0.0567
H	0.4569	-1.0920	-0.4539
O	0.2076	0.6612	0.0567
H	-0.4569	1.0920	-0.4539

Table 30: $\lambda_m = 0.083$ au, $q_1 = 9.0194$ au and $q_2 = 0.0000$ au.

O	-0.2085	-0.6600	0.0562
H	0.4555	-1.0938	-0.4493
O	0.2085	0.6600	0.0562
H	-0.4555	1.0938	-0.4493

Table 31: $\lambda_m = 0.100$ au, $q_1 = 10.7484$ au and $q_2 = 0.0000$ au.

O	-0.2097	-0.6585	0.0555
H	0.4538	-1.0961	-0.4437
O	0.2097	0.6585	0.0555
H	-0.4538	1.0961	-0.4437

Table 32: $\lambda_m = 0.117$ au, $q_1 = 12.4338$ au and $q_2 = 0.0000$ au.

O	-0.2111	-0.6568	0.0547
H	0.4519	-1.0988	-0.4372
O	0.2111	0.6568	0.0547
H	-0.4519	1.0988	-0.4372

Table 33: $\lambda_m = 0.133$ au, $q_1 = 14.0671$ au and $q_2 = 0.0000$ au.

O	-0.2126	-0.6548	0.0537
H	0.4495	-1.1018	-0.4300
O	0.2126	0.6548	0.0537
H	-0.4495	1.1018	-0.4300

Table 34: $\lambda_m = 0.150$ au, $q_1 = 15.6389$ au and $q_2 = 0.0000$ au.

O	-0.2144	-0.6526	0.0527
H	0.4468	-1.1053	-0.4219
O	0.2144	0.6526	0.0527
H	-0.4468	1.1053	-0.4219

References

- (1) Schnappinger, T.; Kowalewski, M. Ab Initio Vibro-Polaritonic Spectra in Strongly Coupled Cavity-Molecule Systems. *J. Chem. Theory Comput.* **2023**, *19*, 9278–9289.
- (2) Rokaj, V.; Welakuh, D. M.; Ruggenthaler, M.; Rubio, A. Light–matter interaction in the long-wavelength limit: no ground-state without dipole self-energy. *J. Phys. B At. Mol. Opt. Phys.* **2018**, *51*, 034005.
- (3) Schäfer, C.; Ruggenthaler, M.; Rokaj, V.; Rubio, A. Relevance of the Quadratic Diamagnetic and Self-Polarization Terms in Cavity Quantum Electrodynamics. *ACS Photonics* **2020**, *7*, 975–990.
- (4) Welakuh, D. M.; Rokaj, V.; Ruggenthaler, M.; Rubio, A. Non-perturbative mass renormalization effects in non-relativistic quantum electrodynamics. **2023**,
- (5) Hopfield, J. J. Theory of the Contribution of Excitons to the Complex Dielectric Constant of Crystals. *Phys. Rev.* **1958**, *112*, 1555–1567.